


# Photoacoustic tweezers generated by multiple superposed laser pulses in air

Guo-Dong Tong(佟国栋), Li-Yan Xu(许立言), Wen-Qi Wang(王雯琦), Jin-Ping He(何晋平), and Jun Xia(夏军)
**Citation:**Chin. Phys. B, 2026, 35 (**3**): 034301. DOI: 10.1088/1674-1056/adf9fd
http://cpb.iphy.ac.cn; http://iopscience.iop.org/cpb

**What follows is a list of articles you may be interested in**

---

## Scheme of negative acoustic radiation force based on a multiple-layered spherical structure

Menyang Gong(宫门阳), Xin Xu(徐鑫), Yupei Qiao(乔玉配), Jiehui Liu(刘杰惠), Aijun He(何爱军), and Xiaozhou Liu(刘晓宙)
Chin. Phys. B, 2024, 33 (**1**): 014302. DOI: 10.1088/1674-1056/acfa80

## Non-invasive and low-artifact *in vivo* brain imaging by using a scanning acoustic-photoacoustic dual mode microscopy

Wentian Chen(陈文天), Chao Tao(陶超), Zizhong Hu(胡仔仲), Songtao Yuan(袁松涛), Qinghuai Liu(刘庆淮), and Xiaojun Liu(刘晓峻)
Chin. Phys. B, 2022, 31 (**4**): 044304. DOI: 10.1088/1674-1056/ac4a6f

## Axial acoustic radiation force on an elastic spherical shell near an impedance boundary for zero-order quasi-Bessel-Gauss beam

Yu-Chen Zang(臧雨宸), Wei-Jun Lin(林伟军), Chang Su(苏畅), and Peng-Fei Wu(吴鹏飞)
Chin. Phys. B, 2021, 30 (**4**): 044301. DOI: 10.1088/1674-1056/abca27

## High-contrast imaging based on wavefront shaping to improve low signal-to-noise ratio photoacoustic signals using superpixel method

Xinjing Lv(吕新晶), Xinyu Xu(徐新羽), Qi Feng(冯祺), Bin Zhang(张彬), Yingchun Ding(丁迎春), Qiang Liu(柳强)
Chin. Phys. B, 2020, 29 (**3**): 034301. DOI: 10.1088/1674-1056/ab6842

## Enhancement of photoacoustic tomography in the tissue with speed-of-sound variance using ultrasound computed tomography

Cheng Ren-Xiang (程任翔), Tao Chao (陶超), Liu Xiao-Jun (刘晓峻)
Chin. Phys. B, 2015, 24 (**11**): 114301. DOI: 10.1088/1674-1056/24/11/114301

---

# Photoacoustic tweezers generated by multiple superposed laser pulses in air

Guo-Dong Tong(佟国栋)[1,2,5], Li-Yan Xu(许立言)[1,2,5], Wen-Qi Wang(王雯琦)[5], Jin-Ping He(何晋平)[1,2,3,4,†], and Jun Xia(夏军)[5,‡]

[1] *Laboratory of Solar and Space Instruments, Nanjing Institute of Astronomical Optics & Technology, Chinese Academy of Sciences, Nanjing* 211135, *China*

[2] *Key Laboratory of Astronomical Optics & Technology CAS, Nanjing Institute of Astronomical Optics & Technology, Chinese Academy of Sciences, Nanjing* 211135, *China*

[3] *University of Chinese Academy of Sciences, Nanjing* 211135, *China*

[4] *University of Chinese Academy of Sciences, Beijing* 100049, *China*

[5] *Joint International Research Laboratory of Information Display and Visualization, School of Electronic Science and Engineering, Southeast University, Nanjing* 210096, *China*

(Received 11 June 2025; revised manuscript received 30 July 2025; accepted manuscript online 11 August 2025)

We propose a novel method for generating photoacoustic tweezers via multi-ultrasonic resonance in air. In this study, a focused ultrashort laser pulse with a 50 ns pulse width is used to generate ultrasonic resonance by transferring thermal energy to atmospheric $H_2O$ in air. Traveling photoacoustic tweezers are generated by modulating the superposition of multiple ultrasonic waves. Through numerical simulations, we obtained the acoustic pressure and temperature fields of the photoacoustic waves. Experimentally, 10 μm microspherical polystyrene particles were placed messily in a 200 μm wide square microfluidic tube. The resulting shapes of the microparticles after manipulation by the photoacoustic tweezers proved that our experimental results align well with theoretical predictions. We demonstrate that the interaction of laser pulses with water vapor can generate both acoustic waves and photoacoustic tweezers.

**Keywords:** acoustic tweezers, laser field modulation, photoacoustic, photoacoustic tweezers, superposition

**PACS:** 43.35.+d, 52.35.Tc, 52.38.–r ,51.40.+p, 52.35.–g

**DOI:** 10.1088/1674-1056/adf9fd **CSTR:** 32038.14.CPB.adf9fd

## 1. Introduction

Acoustic tweezers have attracted significant attention in recent years due to their versatility, label-free operation and non-invasive manipulation capabilities in various microfluidic and biological contexts.[1,2] Unlike optical tweezers, which rely on high-intensity laser beams to trap microscopic objects and are often limited to transparent or dielectric particles,[3–6] acoustic tweezers utilize pressure nodes and antinodes formed by sound fields to exert forces on particles. This allows for the manipulation of larger and more diverse particles, including cells, droplets and even millimeter-scale objects. Moreover, acoustic tweezers present key advantages such as minimal thermal effects, a low risk of photodamage, negligible frictional contact and reduced contamination.[7–12] These features make them highly suitable for sensitive applications, particularly in biological and clinical environments where maintaining cell viability and avoiding material damage are critical.[10,13–15]

Traditional acoustic tweezers are typically categorized into standing wave and traveling wave types,[10,16–18] both based on the interference of sound fields from multiple transducers or reflectors.[6,19–21] However, these systems often require bulky piezoelectric transducers, precise alignment or enclosed liquid environments to support acoustic propagation. These constraints limit their flexibility, integration and operation in open-air or gas-phase systems. To overcome these limitations, researchers have recently explored single-beam acoustic tweezers, which offer greater operational simplicity and portability.[10,22–26] Nevertheless, generating focused and controllable acoustic fields in air, especially at microscale resolution, remains a fundamental challenge due to the low acoustic impedance and high attenuation of air.

To address this, we introduce a new class of acoustic tweezers — photoacoustic tweezers[27,28] — which leverage the interaction between high-frequency pulsed lasers and atmospheric water vapor to generate localized, tunable acoustic fields in air. Unlike traditional acoustic tweezers, this method does not rely on solid transducers or enclosed liquid media. Instead, it converts light into sound directly in the air through the photoacoustic effect, enabling precise, non-invasive manipulation of microparticles in open environments. This novel approach bridges the gap between optical and acoustic trapping techniques, offering a flexible, high-resolution and contactless solution for microscale manipulation in microfluidic

†Corresponding author. E-mail: jphe@niaot.ac.cn

‡Corresponding author. E-mail: xiajun@seu.edu.cn

© 2026 Chinese Physical Society and IOP Publishing Ltd. All rights, including for text and data mining, AI training, and similar technologies, are reserved.

and biomedical systems.

In this study, we propose a novel strategy for generating photoacoustic tweezers in air by utilizing high-frequency pulsed laser beams modulated at gigahertz (GHz) repetition rates. When focused into a water-vapor-rich air environment using a microlens array (MLA), each laser pulse rapidly deposits thermal energy into the surrounding vapor.[7] Due to the large difference between the speed of light and sound, the laser energy is absorbed almost instantaneously, leading to localized thermal expansion and the generation of spherical acoustic waves. When these pulses are delivered at high repetition rates, the resulting acoustic waves overlap and constructively interfere, forming a patterned acoustic field capable of trapping and manipulating microscale particles.

To implement this concept, we designed a system in which multiple focused laser pulses are directed from the left and propagate along the $x$-axis,[29] as illustrated in Fig. 1. These pulses are modeled as Gaussian beams in the simulation, with their spatial focus precisely controlled by a MLA. By adjusting the focal length and position of the MLA, the trapping location of the resulting photoacoustic tweezers can be tuned with high precision.

The laser source operates at a wavelength of 1907 nm and a pulse width of 50 ns, and simulations are conducted in a computational domain measuring 5600 μm in length and 500 μm in width, representing the water-vapor-enriched region of air inside the microfluidic channel. These conditions were chosen to reflect realistic experimental parameters while ensuring sufficient resolution of the generated acoustic fields. The simulated evolution of the acoustic field and its interaction with microparticles form the basis for validating the trapping mechanism described in the subsequent sections.

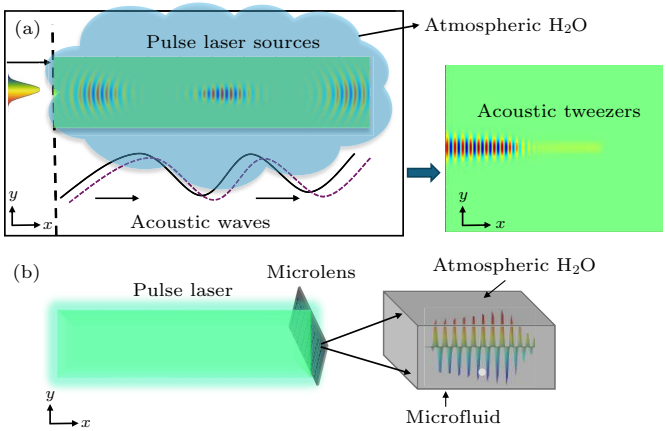



**Fig. 1.** (a) Schematic of the generation of acoustic tweezers using a pulse Gaussian laser. (b) Generation of acoustic waves during propagation of the focused Gaussian laser pulse.

Figure 1 presents a schematic illustration of the acoustic tweezers generated through the interaction between pulsed laser light and water vapor in air. In this mechanism, each ultrashort laser pulse instantaneously transfers thermal energy to the surrounding water vapor. Due to the significant difference in propagation speeds between light and sound, the heated vapor undergoes rapid expansion, leading to the emission of acoustic waves. When the pulsed laser operates at 500 MHz, a total of 500 acoustic wavefronts are sequentially generated within 1000 ns, resulting in constructive superposition.

In our setup, a microlens with a focal length of $f = 5.6$ mm is employed to focus the Gaussian laser pulse along the $+x$ direction. The focal point defines the beam waist, where the pulse profile closely approximates a Gaussian distribution. As shown in Fig. 1(a), multiple pulsed heat sources sequentially traverse the air medium, forming a cumulative superposition of photoacoustic waves. The final acoustic field distribution, constituting the acoustic tweezers, is illustrated in Fig. 1(b).

## 2. Theory and simulation of photoacoustic resonance in air

### 2.1. Generation of photoacoustic waves

The physical mechanism linking pulsed-laser-induced heating and ultrasonic resonance is governed by the photoacoustic effect. When an ultrashort laser pulse propagates through air and is absorbed by water vapor molecules, it causes an instantaneous localized temperature rise due to rapid energy transfer. This thermal expansion induces a pressure increase, generating an acoustic wave that propagates outward from the heated region. Because the speed of light far exceeds the speed of sound, multiple acoustic waves from sequential laser pulses can superimpose constructively when the pulse repetition rate is sufficiently high. This superposition leads to the formation of ultrasonic resonance in air.

Here, the acoustic field is analyzed by the time domain analysis of Gaussian pulse simulation through COMSOL Multiphysics.

The electric field of the Gaussian beam's electromagnetic mode[30,31] is expressed as follows:

$$\begin{aligned} \boldsymbol{E}(r,x)_{\text{single}} = {} & E_0\hat{\boldsymbol{z}}\frac{\omega_0}{\omega(x)}\exp\left(\frac{-r^2}{\omega(x)^2}\right) \\ & \times\exp\left(-\mathrm{i}\left(kx+k\frac{r^2}{2R(x)}-\psi(x)\right)\right) \\ & \times\exp(\mathrm{i}\omega t)\exp\left(-\frac{(t-t_0)^2}{\tau^2}\right). \end{aligned} \tag{1}$$

Here, $r$ denotes the radial distance from the beam's central axis, i is the imaginary unit and $E = E(0,0)$ represents the electric field amplitude at the origin ($r = 0$, $x = 0$). The term $\omega(x)$ denotes the beam radius as a function of the propagation distance $x$, $R(x)$ is the radius of curvature of the beam and $\psi(x)$ is the Gouy phase shift. The temporal profile of the laser pulse is characterized by a Gaussian envelope, described by the term $\exp\left(-(t-t_0)^2/\tau^2\right)$, where $\tau$ is the pulse width and $t_0$ is the temporal delay introduced in the simulation.

To prevent numerical instability or inaccuracies at the start of the simulation, we set $t_0 = 3\tau$. This choice ensures that the peak of the laser pulse occurs at $t = 3\tau$ while the initial field amplitude at $t = 0$ remains sufficiently small. If $t_0 < 3\tau$ the initial field amplitude becomes too large, potentially causing steep field gradients and instability in the numerical solution as well as an inaccurate representation of the pulse's smooth onset. Conversely, choosing $t_0 \gg 3\tau$ would result in a near-zero initial field amplitude, which although numerically stable introduces unnecessary computational overheads due to a prolonged period of negligible field before the pulse peak arrives. Therefore, setting $t_0 = 3\tau$ provides a well-balanced approach: it avoids excessive initial field amplitudes that could destabilize the simulation while also ensuring computational efficiency by allowing the pulse to reach its peak within a reasonable time frame. This parameter selection was validated through extensive simulation testing.

The propagation of multiple Gaussian laser pulses along the $+x$ direction is governed by the following equation:[32,33]

$$\begin{aligned} &\boldsymbol{E}(r,x)_{\text{multi}} \\ &= E_0\hat{z}\frac{\omega_0}{\omega(x)}\exp\left(\frac{-r^2}{\omega(x)^2}\right) \\ &\quad\times\exp\left(-\mathrm{i}\left(kx+k\frac{r^2}{2R(x)}-\psi(x)\right)\right) \\ &\quad\times\exp(\mathrm{i}\omega t)\sum_0^n\exp\left(\frac{-(t-(t_0+n\Delta t))^2}{\tau^2}\right), \end{aligned} \tag{2}$$

where $n$ is the number of pulses emitted by the laser, $n = t/\Delta t$, and $\Delta t$ is the period of the Gaussian pulse laser. According to $I(r,x) = \frac{|E(r,x)|^2}{2\eta}$, the intensity of the single Gaussian pulse equation is

$$I(r,x)_{\text{single}} = I_0\left(\frac{w_0}{w(x)}\right)^2\exp\left(\frac{-2r^2}{w(x)^2}\right)\exp\left(-2\frac{(t-t_0)^2}{\tau^2}\right) \tag{3}$$

and the intensity of the multiple Gaussian pulses equation is

$$\begin{aligned} I(r,x)_{\text{multi}} &= I_0\left(\frac{w_0}{w(x)}\right)^2\exp\left(\frac{-2r^2}{w(x)^2}\right)\exp\left(-2\frac{(t-t_0)^2}{\tau^2}\right) \\ &\quad\times\sum_0^n\exp\left(-2\frac{\left(t-\frac{x}{C}-(t_0+n\Delta t)\right)^2}{\tau^2}\right), \end{aligned} \tag{4}$$

$$Q_0 = I(r,x)_{\text{multi}}\alpha, \tag{5}$$

where $\alpha$ is the absorption coefficient of the laser in water vapor, with $\alpha = 0.04\ \text{m}^{-1}$.[34] The reference atmospheric pressure of the air used in this paper is $p_{\text{ref}} = 20\ \mu\text{Pa}$.

By using the intensity equation for multiple pulses and the absorption coefficient of water vapor, we can calculate the heat energy transferred from the pulsed laser source to the water vapor.[33,34] Therefore, the equation for laser-induced heat transfer is

$$\begin{cases} d_z\rho C_{\text{p}}\frac{\partial T}{\partial t} + d_z\rho C_{\text{p}}\boldsymbol{u}\cdot\nabla T + \nabla\cdot\boldsymbol{q} = d_zQ + q_0 + d_zQ_{\text{ted}}, \\ \boldsymbol{q} = -d_zk\nabla T, \end{cases} \tag{6}$$

where $d_z$ is the thickness of the simulation area, $\rho$ is the density of water vapor ($\rho = 0.5976\ \text{kg}\cdot\text{m}^{-3}$), $T$ is the temperature, $C_{\text{p}}$ is the specific heat capacity at constant pressure and $Q$ is the total monopole domain source, typically associated with laser heat sources. In the context of heat conduction, this can be expressed as the heat source distribution within the volume, i.e., the heat generated per unit volume. $\boldsymbol{u}$ is the heat source diffusion velocity vector, $\boldsymbol{q}$ is the total dipole source, representing the distribution in the region due to heat flow or other vector fields, $q_0$ is the inward heat flux and $k$ is the wave number, The size of the calculated action area is 5600 μm×500 μm.

Acoustic pressure is a commonly used physical quantity for measuring sound waves. By measuring pressure, we can analyze the field intensity distribution and sound intensity of the waves. The relationship between the pressure equation and the heat sources is given by

$$\begin{cases} Q_{\text{m}} = \frac{1}{\rho c^2}\frac{\partial^2 p_{\text{t}}}{\partial t^2} + \nabla\cdot\left(-\frac{1}{\rho}(\nabla p_{\text{t}} - \boldsymbol{q}_{\text{d}})\right), \\ p_{\text{t}} = p + p_{\text{b}}, \end{cases} \tag{7}$$

where $c$ is the speed of propagation of sound waves in air ($c = 343\ \text{s}^{-1}$), $p_{\text{b}}$ is the background sound pressure, $\boldsymbol{q}_{\text{d}}$ is the volume force source, $p$ is the scattered sound pressure and $p_{\text{t}}$ is the total sound pressure:

$$Q_{\text{m}} = \frac{\alpha_{\text{p}}}{\rho C_{\text{p}}}\frac{\partial Q_{\text{heat}}}{\partial t}, \tag{8}$$

$$\alpha_{\text{p}} = \frac{1}{c}\sqrt{\frac{C_{\text{p}}(\gamma-1)}{T}}. \tag{9}$$

Here, $\alpha_{\text{p}}$ denotes the isobaric thermal expansion coefficient, $Q_{\text{m}}$ represents the total heat source, $\gamma$ is the specific heat ratio and $Q_{\text{heat}}$ refers to the thermal energy transferred from the laser pulse to the water vapor.

Using the heat transfer equations and the established relationship between pressure and heat input, we simulated and analyzed the physical quantities, such as the acoustic pressure, generated when multiple Gaussian laser pulses pass through the interaction region. These simulations were performed using COMSOL Multiphysics, and the resulting acoustic field distribution is shown in Fig. 2(b). In this simulation, the laser pulse propagates along the $+x$ direction.

Due to the much higher speed of light compared with that of sound, the photoacoustic resonance produced by the initial laser pulse does not fully dissipate before the subsequent pulse generates a new wave. As a result, the repetition rate (or frequency) of the pulsed laser becomes a critical factor influencing the degree of acoustic wave superposition. To accurately model and analyze this effect, both the amplitude and phase of each photoacoustic wave must be taken into account.

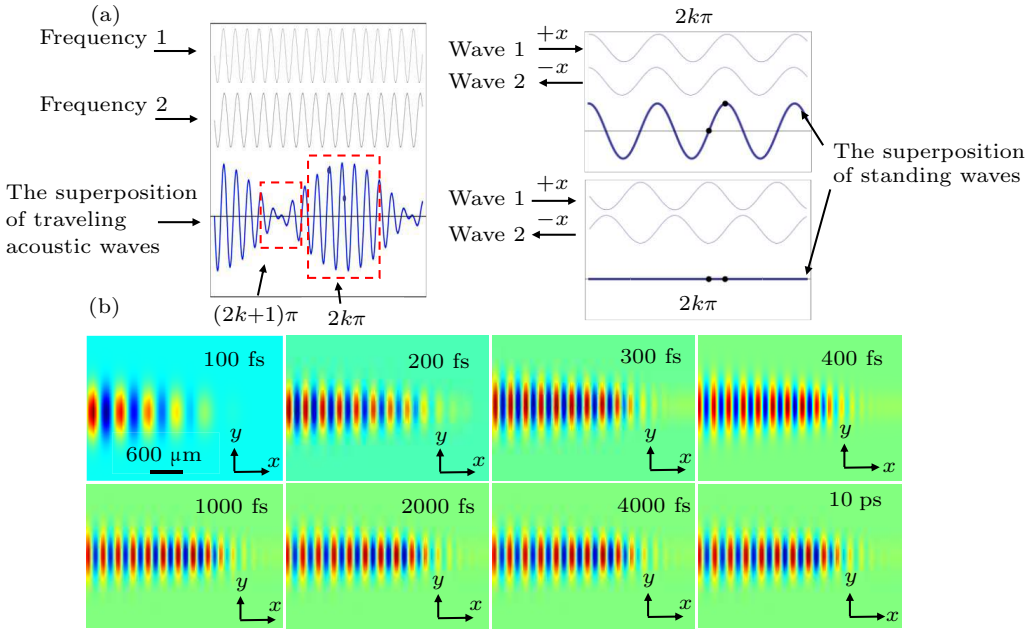



**Fig. 2.** (a) The principle of superposition of two acoustic waves with different propagation directions and different phases. (b) Simulation of the generation of photoacoustic tweezers by superposition of photoacoustic waves with times from 100 fs to 10 ps by COMSOL Multiple software.

Multiple laser pulses propagating through air generate photoacoustic resonances that travel outward in the direction of laser propagation, as illustrated in Fig. 2. Since the speed of light is significantly greater than the speed of sound each laser pulse effectively creates an individual acoustic wave, resulting in a total of $n$ superimposed shock waves when $n$ pulses are applied.[35,36] These shock waves are distributed along the $x$-axis, leading to a complex superposition pattern in both the forward and backward directions (see the supplementary material for detailed derivation).

Simulations conducted using COMSOL Multiphysics revealed that in the time range of 100 fs to 10 ps, complex superpositions of multiple acoustic waves form traveling-wave photoacoustic tweezers. The simulation parameters were set to a 50 ns pulse width, 300 W average laser power and a 50 GHz repetition rate. The absorption coefficient of atmospheric water vapor was taken as 0.04 $m^{-1}$.[34]

When high-frequency modulated laser pulses are focused into ambient air, their energy is primarily absorbed by water vapor molecules due to strong infrared absorption characteristics (1907 nm). This absorption leads to a rapid and localized temperature rise within the illuminated region. Because the pulse duration is extremely short (on the order of nanoseconds), thermal expansion of the heated vapor occurs faster than thermal diffusion, resulting in a nearly adiabatic process.

The sudden thermal expansion induces a sharp pressure increase, which radiates outward in the form of a photoacoustic wave. Due to the high repetition rate of the laser pulses (e.g., 500 MHz), the resulting acoustic waves are emitted sequentially and superimpose in both time and space. This leads to constructive interference of the pressure fields, forming a traveling, spatially focused Gaussian-shaped acoustic wave.

The superimposed acoustic waves create a localized acoustic radiation force field in air. When particles such as polystyrene (PS) microspheres are present in the interaction region, they experience gradient and scattering forces due to the acoustic pressure field. These forces can trap and manipulate the particles, functioning similarly to conventional acoustic tweezers.

The formation of photoacoustic tweezers is strongly influenced by the temporal spacing between pulses, the beam's focusing geometry and the physical properties of the absorbing medium (i.e., the water vapor content). Figure 1 illustrates this mechanism, while figure 2(b) shows the pressure field resulting from multiple Gaussian pulses, as simulated using COMSOL Multiphysics.

### 2.2. Theory of photoacoustic wave manipulation of microparticles

Previous studies have shown that ultrasonic acoustic tweezers with a resonance frequency of tens of MHz can manipulate microparticles ranging from tens to hundreds of micrometers in size in water.[10,37–40] In this study, we employ a focused pulsed laser to interact with water vapor, generating Gaussian photoacoustic waves in air. In order to study the overall trend and physical mechanism of acoustic wave superposition, we sampled and simulated a photoacoustic waveform with a modulation frequency of 50 GHz (Fig. 2). Considering our existing experimental conditions, the highest frequency of our laser is 1 GHz and a simulation analysis of the photoacoustic wave generated by a 1 GHz pulsed laser frequency was conducted. The diameter of the PS microparticles is 10 μm. Given that photoacoustic waves are highly focused, we first

obtain the incident wave $p_{\mathrm{i}}$ using the spherical function

$$p_{\mathrm{i}} = p_0 \sum_{n=0}^{\infty} G_n (2n+1)\, \mathrm{i}^n j_n (kf(r,\theta)) P_n(\cos\theta), \quad (10)$$

where $f(r,\theta)$ is a focal distance and angle correlation function, which is used to better describe the wavefront distortion under strong focusing conditions, $G_n$ is the expansion coefficient, $j_n$ is the spherical Bessel function and $P_n$ is the Legendre polynomial. Assuming that the Gaussian sound wave is symmetrical about the $x$-axis, the scattered wave in the liquid in spherical coordinates $p_{\mathrm{s}}$ is

$$p_{\mathrm{s}} = p_0 \sum_{n=0}^{\infty} G_n (2n+1)\, \mathrm{i}^n A_{n,\mathrm{s}} h_n^{(1)} (kf(r,\theta)) P_n(\cos\theta), \quad (11)$$

where $A_{n,\mathrm{s}}$ is the scattering coefficient. The density of the medium is $\rho_0$ and the velocity is $c_0$. The scattering coefficient $A_{n,\mathrm{s}}$ obtained using the above two equations is

$$A_{n,\mathrm{s}} = -\frac{j_n'(ka)}{h_n^{(1)'}(ka)}, \quad (12)$$

where $h_n^{(1)}(ka)$ is the spherical Hankel function of the first kind, describing the outgoing wave, $j_n(ka)$ is the spherical Bessel function of the first kind, describing the regular solution in inside the sphere, and $j_n'(ka)$ is the derivative of the spherical Bessel function with respect to its argument. Substituting the above Eq. (14) into the scattered wave function Eq. (13) and combining with the incident wave function,[38] the total acoustic pressure of the particle can be obtained as

$$p_{\mathrm{total}} = p_0 \sum_{n=0}^{\infty} G_n (2n+1)\, \mathrm{i}^n \times \left[ j_n(kr) + A_{n,\mathrm{s}} h_n^{(1)}(kr) \right] P_n(\cos\theta). \quad (13)$$

The radiation force of photoacoustic tweezers is determined by the energy and momentum exchange between the sound wave and the particle. The radiation force is divided into the gradient force $F_{\mathrm{grad}}$ and the scattering force $F_{\mathrm{scat}}$. The gradient force comes from the influence of the sound pressure gradient, which is calculated by the square distribution of the sound pressure

$$F_{\mathrm{grad}} = \frac{1}{2} \nabla \left( \frac{p_{\mathrm{i}}^2}{\rho_0 c_0^2} \right), \quad (14)$$

where $\rho_0$ is the density of the medium, $c_0$ is the speed of sound, $p_{\mathrm{i}}$ is the incident wave pressure and the gradient acts on the energy density of the incident wave.

The scattering force is generated by the interaction between the particle surface and the acoustic field, and is expressed as follows:

$$F_{\mathrm{scat}} = \sum_{n=0}^{\infty} (2n+1) |A_{n,\mathrm{s}}|^2 \frac{W}{c_0} P_n(\cos\theta), \quad (15)$$

where $W$ is the energy density of the sound field.

The radiation force $F_{\mathrm{rad}}$ is the sum of the gradient force and the scattering force, that is

$$F_{\mathrm{rad}} = F_{\mathrm{scat}} + F_{\mathrm{grad}}. \quad (16)$$

Expanding this, we end up with

$$F_{\mathrm{rad}} = -\nabla \left( \frac{p_{\mathrm{i}}^2}{2\rho_0 c_0^2} \right) + \sum_{n=0}^{\infty} (2n+1) |A_{n,\mathrm{s}}|^2 \frac{k}{\rho_0 c_0} P_n(\cos\theta). \quad (17)$$

In deriving Eq. (17), we assume that the particle is much smaller than the acoustic wavelength (Rayleigh scattering regime) and the surrounding medium is an inviscid, lossless fluid (air). The radiation force is separated into a gradient force, which originates from the spatial variation of the acoustic energy density, and a scattering force, resulting from momentum transfer due to wave–particle interaction. Only the dominant terms in the multipole expansion are retained for analytical tractability, leading to a simplified expression for $F_{\mathrm{rad}}$.

To ensure the stability of the photoacoustic tweezers, the gradient force must be sufficiently large to overcome the scattering force. The condition for stable trapping is that the particle should be attracted to the region of highest acoustic field intensity and not be repelled by the scattering force.

By adjusting the frequency and intensity $p_0$ of the incident wave, we can control the relative magnitudes of the gradient and scattering forces, ensuring that the particle remains stable within the hotspot of the acoustic field. The final expression for the capture force is as follows:

$$F_{\mathrm{trap}} = \frac{V \rho_0 |p_0|^2}{c_0^2 r^3} + \sum_{n=0}^{\infty} (2n+1) |A_{n,\mathrm{s}}|^2 \frac{k}{\rho_0 c_0} P_n(\cos\theta). \quad (18)$$

## 3. Results and discussion

Through calculation and simulation we find that the shape of the generated shock wave is influenced by both the energy of a single laser pulse and the repetition frequency of the laser pulses. The phenomenon of superposition of the shock wave only occurs when both the single pulse energy and the repetition frequency of the pulsed laser meet the required conditions simultaneously, as illustrated in Fig. 3.

In our setup, laser pulses with a width of 50 ns interact with atmospheric water vapor to produce Gaussian-distributed acoustic fields. By modulating the repetition rate of the laser (e.g., 1 GHz in experiments), we control the temporal overlap and phase alignment of these waves, allowing the formation of resonant acoustic pressure patterns. These resonant fields exert acoustic radiation forces on nearby microparticles, forming the basis of the photoacoustic tweezer mechanism proposed in this study.

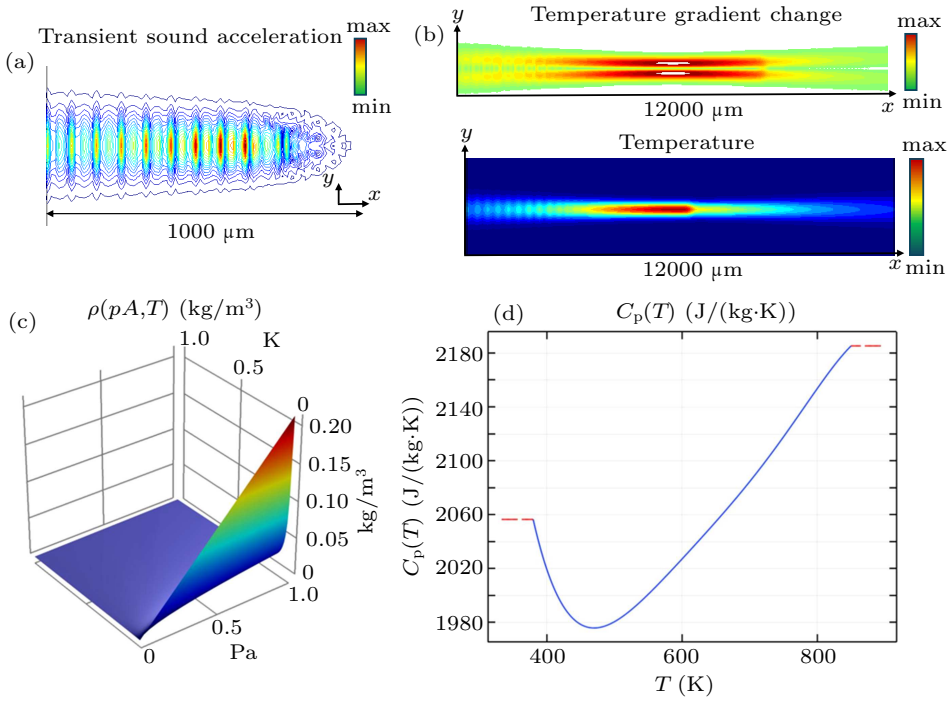



**Fig. 3.** Analysis of different physical quantities of the acoustic tweezers. (a) Distribution of the acceleration of the acoustic waves propagating along the $x$-direction. (b) The change of the temperature gradient of the acoustic tweezers and temperature change after each laser pulse heat source passes through. (c) The pressure density of the generated air disturbance. (d) The constant pressure heat capacity distribution of changes with temperature at different locations (the absolute temperature is set to 293.15 K).

To investigate the effects of different frequencies and to ensure consistency between the simulation and experimental conditions, we conducted extensive studies across a range of laser pulse frequencies. Specifically, we employed COMSOL Multiphysics to simulate the photoacoustic field generated by a 1 GHz pulsed laser within a 5600 μm section of the microfluidic tube, as shown in Fig. 4. The simulation results confirm that a photoacoustic field is successfully established within this region. Moreover, the spatial distribution of the field exhibits alternating high and low acoustic pressure zones, closely resembling the characteristic structure of photoacoustic tweezers.

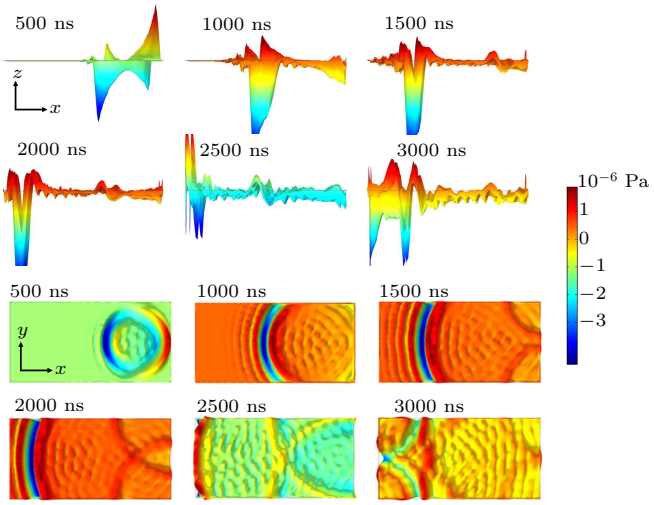



**Fig. 4.** Image of photoacoustic pressure in the $x$–$z$ direction generated by the interaction of a 1 GHz pulsed laser with atmospheric $H_2O$.

To further illustrate the similarity between the generated photoacoustic waves and acoustic tweezers, we quantitatively analyzed both the photoacoustic pressure and the photoacoustic radiation force produced by the photoacoustic tweezers and compared them with acoustic tweezers under identical conditions. We normalized the photoacoustic radiation force and defined it in terms of a dimensionless radiation force. We set $F$ to represent the actual calculated photoacoustic radiation force and $F_{\text{ref}}$ as the reference force value. The dimensionless photoacoustic radiation force, denoted as $F^*$, is defined as

$$F^* = \frac{F}{F_{\text{ref}}}, \tag{19}$$

where $F_{\text{ref}}$ is typically chosen as the maximum value $F_{\max}$ of the photoacoustic radiation force, or the theoretical peak radiation force. The range of values of $F^*$ is set to $-1$ to 1, representing the directionality of the radiation force, i.e., the attractive and repulsive forces in the trapping behavior. Figures 5(a) and 5(b) compare the photoacoustic pressure and radiation force of the photoacoustic tweezers under the excitation of a single pulse energy of 2 μJ.

Additionally, we compared and analyzed the vector intensity of the focused traveling wave photoacoustic tweezers and acoustic tweezers, and normalized the vector field. The normalized vector intensity field is given by

$$I_{\text{norm}} = \frac{I}{\max(|I|)}, \tag{20}$$

where $I$ is the unplanned vector strength and $\max(|I|)$ is the maximum value of the field strength. Therefore, the normalized formula for the traveling wave photoacoustic tweezers

field is

$$I_{\mathrm{PA,norm}} = \frac{I_{\mathrm{PA}}}{\max\left(|I_{\mathrm{PA}}|\right)} = \frac{\frac{1}{2\rho_0 c_0}|p_{\mathrm{PA}}|^2}{\max\left(\frac{1}{2\rho_0 c_0}|p_{\mathrm{PA}}|^2\right)}\hat{k}. \quad (21)$$

Since $|p_{\mathrm{PA}}| = p_{\mathrm{i}}$, the vector direction remains unchanged after normalization, and the modulus is normalized to [0, 1].

The normalized formula of the traveling wave acoustic tweezers field is

$$I_{\mathrm{A,norm}} = \frac{I_{\mathrm{A}}}{\max\left(|I_{\mathrm{A}}|\right)} = \frac{\frac{1}{2\rho_0 c_0}|p_{\mathrm{A}}|^2}{\max\left(\frac{1}{2\rho_0 c_0}|p_{\mathrm{A}}|^2\right)}\hat{k}. \quad (22)$$

Similarly, the normalized modulus is [0, 1]. Figures 6(c) and 6(d) show the normalized vector field intensity analysis, where the arrow direction represents the directionality of the vector field.

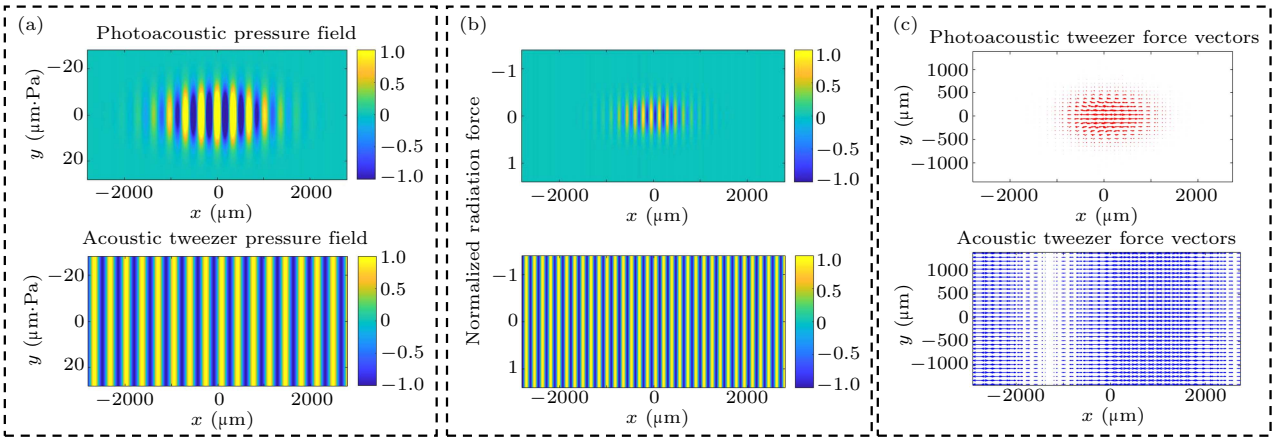



**Fig. 5.** (a) Comparison between photoacoustic pressure and acoustic tweezers pressure (the single pulse laser energy is 2 μJ). (b) Comparison between the normalized photoacoustic radiation force and the acoustic tweezers radiation force. (c) Normalized image of the vector field intensity of the focused traveling-wave photoacoustic tweezers.

We calculated the correlation coefficient and mean square error (MSE) of the acoustic pressure and acoustic radiation force curves. The correlation coefficient quantifies the strength and direction of the linear relationship between the distributions, while the MSE measures the average squared difference between them, as shown in Fig. 5. The correlation coefficient for the acoustic pressure value curve in Fig. 5(a) is 0.06542, with a MSE of 0.9264. The correlation coefficient for the radiation force curve in Fig. 5(b) is 0.04653, with a MSE of 0.7803. The relatively low MSE and high correlation coefficient indicate a strong similarity between the intensity distribution of the photoacoustic field and that of the photoacoustic tweezers. The small average squared difference further confirms this similarity. Figures 5(c) and 5(d) show the normalized vector intensity images of photoacoustic tweezers and acoustic tweezers in the 5600 μm and 500 μm ranges, respectively. From these images it is clear that when focused photoacoustic tweezers produce the same incident wave pressure as acoustic tweezers they generate very similar vector fields. Therefore, the data presented in Fig. 1 demonstrates that photoacoustic tweezers closely resemble acoustic tweezers in form.

With reference to the preceding simulations and numerical analyses, we conducted experiments to validate the photoacoustic tweezing effect. PS microspheres with a diameter of 10 μm were introduced into an integrated microfluidic tube, where they were initially randomly distributed, as shown in Fig. 6. The experimental platform utilized a 200 μm wide square microfluidic channel (Microfluidic ChipShop), featuring four channels integrated with eight identical microfluidic tubes. A MLA (MLA150-7AR(-M), Thorlabs) with dimensions of 10 mm×10 mm×1.2 mm arranged in a square grid was employed. Each microlens has a focal length of 5.6 mm, enabling accurate focusing of the laser pulses into the microchannel.

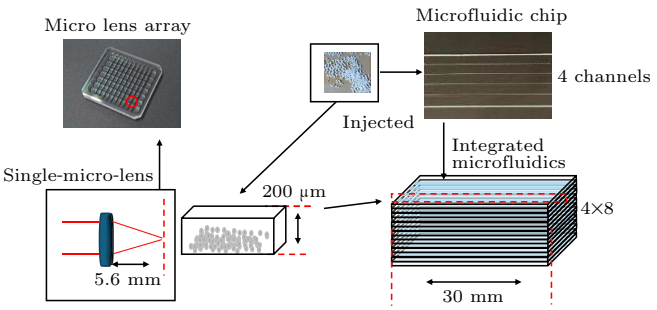



**Fig. 6.** The experimental setup integrating eight microfluidic chips. 10 μm PS microspheres are injected into the microfluidic tube, where the focal length of the microlens is 5600 μm and the diameter of the microlens is 200 μm.

In the experiment, a CCD camera (Balser acA1440-220uc, Germany) was positioned at the lens's focal point. Through multiple trials, we observed that the acoustic tweezers could not move the PS particles on the water surface, suggesting that the force exerted by the acoustic tweezers was smaller than the viscosity or surface tension of the water acting on the particles. As a result, we did not place the PS particles

in water for this experiment.[9,39] All experiments were performed under ambient laboratory conditions with a room temperature of approximately 25 °C and relative humidity ranging from 45% to 55%. No active humidity control was applied. Our findings indicate that acoustic tweezers can manipulate and transport PS microparticles in a glass box without water. Fig. 7(c) shows the arrangement of the PS microparticles after manipulation by acoustic waves, which corresponds to the simulated result for the acoustic tweezers shown in Fig. 7(b). Experimentally, the effective control range of the microparticles was found to be approximately 5600 μm. Beyond this range, the strength of the acoustic tweezers weakens significantly, with the strongest effects near the focal point and diminishing along the *x*-axis. The experimental setup and graph of the results are presented in Fig. 7.

In the experimental results presented in Fig. 7, we observe that in a single beam of sound waves it is challenging to obtain an explicit expression for the acoustic contrast factor. However, in the Rayleigh limit, for most cases of acoustic tweezers capturing microparticles, particles with positive acoustic contrast factors are captured at the minimum pressure point while particles with negative acoustic contrast factors are captured at the maximum pressure point. To quantitatively evaluate the trapping performance shown in Fig. 7, we tracked the displacement of PS particles before and after photoacoustic excitation. The typical displacement toward the pressure focal region is measured to be approximately 15 μm within 200 ms. The standard deviation of the particles' final position across five repeated trials was ±1.8 μm, indicating stable trapping. Additionally, based on the displacement–restoring force profile derived from the simulated acoustic gradient, the estimated trapping stiffness is approximately 1.2 pN·μm$^{-1}$ under current parameters. This confirms that the photoacoustic tweezers can produce sufficient radiation force to confine microparticles with high spatial precision. These findings were verified experimentally, confirming the consistency between theory and experiment.

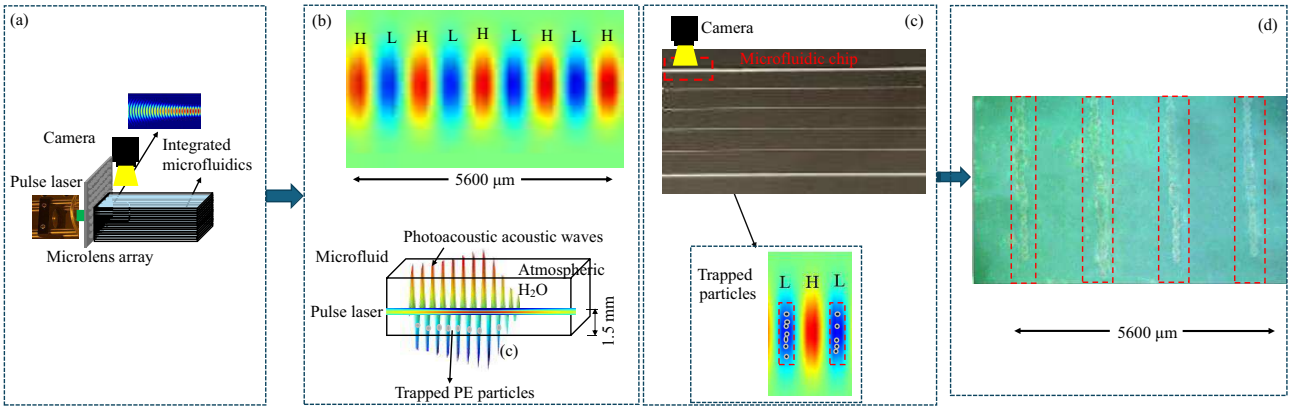



**Fig. 7.** (a), (c) Experimental setup for generating acoustic tweezers. (b) A simulated focused Gaussian laser pulse with a repetition rate of 1 GHz interacts with atmospheric $H_2O$ near the focal point to generate an acoustic pressure image with COMSOL Multiphysics software. (d) The stripe pattern of PS microspheres with diameters of several micrometers formed by the photoacoustic tweezers (1 GHz).

Furthermore, when the average power of the laser is 200 W, the energy of a single pulse is 20 mJ and the repetition frequency is 10 kHz, it was found that the superposition of acoustic waves could not be generated through COMSOL Multiphysics simulation. The interval between each pulse is $1 \times 10^{-4}$ s. According to the shock wave propagation equation described earlier, the first shock wave has dissipated before the second one arrives. Therefore, for a pulsed laser with a repetition rate of 10 kHz, it is difficult to achieve superposition of shock waves at the currently achievable maximum energy of a single pulse.

In addition, the influence of thermal diffusion on trapping performance was considered. Since the laser pulse width (50 ns) is much shorter than the characteristic thermal diffusion time in air, the system operates within the thermal confinement regime. Consequently, the heat remains localized near the absorption region during pressure wave generation, which ensures effective acoustic excitation and minimizes deterioration of trapping force due to heat spread.

## 4. Conclusion and perspectives

In summary, we conducted a comprehensive investigation of shock wave generation resulting from the interaction between a 50 ns pulsed laser and atmospheric $H_2O$, through both simulation and experiment. We analyzed the propagation characteristics and waveform of the resulting shock waves in air, and systematically examined the influence of energy and pulse repetition frequency on wave superposition.

Using theoretical analysis and COMSOL-based simulations, we explored various mechanisms of acoustic resonance. Our findings show that when the pulsed laser has a repetition rate exceeding 1 GHz and each pulse carries 2 μJ of energy, superimposed shock waves can form near the focal point, exhibiting features characteristic of traveling-wave photoacoustic tweezers. Experimentally, we verified the existence of

1 GHz photoacoustic tweezers by observing the arrangement of 10 μm PS microparticles, which aligned in patterns consistent with acoustic trapping. In contrast, at repetition rates below 1 MHz, the same pulse energy is insufficient to generate stable photoacoustic tweezers.

The spatial position of shock wave generation was also found to depend on both single-pulse energy and repetition frequency. With constant average laser power, increasing the repetition rate leads to a decrease in per-pulse energy. As a result, at 1 MHz the shock wave forms at the focal region, while at 50 MHz it shifts toward the laser's initial incidence point. This indicates that adequate single-pulse energy is essential to produce effective shock wave superposition at the focus.

These theoretical and experimental insights into shock wave dynamics provide a valuable foundation for future research into laser–matter interactions in air, as well as the development of high-frequency photoacoustic manipulation techniques.

## Acknowledgements

This work was supported by the National Key Research and Development Program of China (Grant No. 2024YFA1612002), the National Natural Science Foundation of China (Grant Nos. 12503094, 11973009, and 11933005), the Jiangsu Provincial Key Research and Development Program (Grant No. BE2023080), the fund from Chinese Academy of Sciences (Grant No. KGFZD-145-23-04-03), China Postdoctoral Science Found (Grant No. 2025M773196), and CAS Young Entrepreneurship Program of Nanjing Institute of Astronomical Optics and Technology, Chinese Academy of Sciences (Grant No. E5Q2500005).

## References

[1] McGloin D 2006 *Philos Trans. A Math. Phys. Eng. Sci.* **364** 3521
[2] Yang Y, Ren Y X, Chen M, Arita Y and Rosales-Guzmán C 2021 *Adv. Photonics* **3** 03400
[3] Zemánek P, Jonáš A, Šrámek L and Liška M 1998 *Opt. Commun.* **151** 273
[4] Liu S, Lin L and Sun H B 2021 *ACS Nano* **15** 5925
[5] Otte E and Denz C 2020 *Appl. Phys. Rev.* **7** 041308
[6] Courtney C R, Demore C E, Wu H, Grinenko A, Wilcox P D, Cochran S and Drinkwater B W 2014 *Appl. Phys. Lett.* **104** 154103
[7] Gong M, Xu X, Qiao Y, Liu J, He A and Liu X 2024 *Chin. Phys. B* **33** 14302
[8] Li J, Crivoi A, Peng X, Shen L, Pu Y, Fan Z and Cummer S A 2021 *Commun. Phys.* **4** 113
[9] Baudoin M and Thomas J L 2020 *Annu. Rev. Fluid Mech.* **52** 205
[10] Ozcelik A, Rufo J, Guo F, Gu Y, Li P, Lata J and Huang T J 2018 *Nat. Methods* **15** 1021
[11] Foresti D, Nabavi M, Klingauf M, Ferrari A and Poulikakos D 2013 *Proc. Natl. Acad. Sci. USA* **110** 12549
[12] Foresti D and Poulikakos D 2014 *Phys. Rev. Lett.* **112** 24301
[13] Kawamoto H and Seki K 2004 *NIP & Digit. Fabr. Conf.* pp. 1019–1026
[14] Kawamoto H and Hasegawa N 2004 *J. Imaging Sci. Technol.* **48** 404
[15] Hirayama R, Plasencia D M, Masuda N and Subramanian S 2020 *Proc. SPIE* 11463, Optical Trapping and Optical Micromanipulation XVII, 114630Q
[16] Orban C, Morrison J T, Chowdhury E A, Nees J A, Frische K, Feister S and Roquemore W M 2015 *Phys. Plasmas* **22** 23110
[17] Bernassau A L, Glynne-Jones P, Gesellchen F, Riehle M, Hill M and Cumming D R S 2014 *Ultrasonics* **54** 268
[18] Peng X, He W, Xin F, Genin G M and Lu T J 2020 *J. Mech. Phys. Solids* **145** 104134
[19] Tu Y L, Chen S J and Hwang Y R 2016 *Sensors* **16** 1973
[20] Yan N, Di W L, Hong Z Y, Xie W J and Wei B B 2019 *Chin. Phys. Lett.* **36** 34303
[21] Tong G D, Xia J, Zhong H F, Liu S, Wu J, Zhao W Q, Wu Z H, Zhang H, Dong C K and Du B T 2022 *Phys. Fluids* **34** 17110
[22] Babjak R and Psikal J 2021 *Phys. Plasmas* **28** 3107
[23] Li Y, Lee C, Chen R, Zhou Q and Shung K K 2014 *Appl. Phys. Lett.* **105** 173701
[24] Silva G T and Baggio A L 2015 *Ultrasonics* **56** 449
[25] Baresch D, Thomas J L and Marchiano R 2016 *Phys. Rev. Lett.* **116** 24301
[26] Courtney C R, Ong C K, Drinkwater B W, Wilcox P D, Demore C, Cochran S, Glynne-Jones P and Hill M 2010 *J. Acoust. Soc. Am.* **128** EL195
[27] Zharov V P, Malinsky T V and Kurten R C 2005 *J. Phys. D: Appl. Phys.* **38** 2662
[28] Zharov V P, Malinsky T V and Alekhnovich V 2003 *Rev. Sci. Instrum.* **74** 779
[29] Peng Q, Peng Z, Lang Y, Zhu Y, Zhang D, Lü Z and Zhao Z 2022 *Chin. Phys. Lett.* **39** 53301
[30] Misra S, Mishra S K and Sodha M S 2013 *Phys. Plasmas* **20** 103105
[31] Seshadri S R 1998 *J. Opt. Soc. Am. A* **15** 2712
[32] Sprangle P, Penano J R and Hafizi B 2022 *Phys. Rev. E* **66** 46418
[33] Worku N G and Gross H 2019 *J. Opt. Soc. Am. A* **37** 98
[34] Park H K, Kim D, Grigoropoulos C P and Tam A C 1996 *J. Appl. Phys.* **80** 4072
[35] Kim D, Ye M and Grigoropoulos C P 1998 *Appl. Phys. A* **67** 169
[36] Ohiri K A, Kelly S T, Motschman J D, Lin K H, Wood K C and Yellen B B 2018 *Lab on a Chip* **18** 2124
[37] Guo X and Zhu R 2013 *In The 7th IEEE International Conference on Nano/Molecular Medicine and Engineering*, pp. 125–129
[38] Woerdemann M, Alpmann C, Esseling M and Denz C 2013 *Laser & Photonics Reviews* **7** 839
[39] Collins D J, Devendran C, Ma Z, Ng J W, Neild A and Ai Y 2016 *Sci. Adv.* **2** e1600089
[40] Thomas J L, Marchiano R and Baresch D 2017 *J. Quant. Spectrosc. Radiat. Transf.* **195** 55